

Land Cover Change Detection at Subpixel Resolution With a Hopfield Neural Network

Qunming Wang, Wenzhong Shi, Peter M. Atkinson, and Zhongbin Li, *Student Member, IEEE*

Abstract—In this paper, a new subpixel resolution land cover change detection (LCCD) method based on the Hopfield neural network (HNN) is proposed. The new method borrows information from a known fine spatial resolution land cover map (FSRM) representing one date for subpixel mapping (SPM) from a coarse spatial resolution image on another, closer date. It is implemented by using the thematic information in the FSRM to modify the initialization of neuron values in the original HNN. The predicted SPM result was compared to the original FSRM to achieve subpixel resolution LCCD. The proposed method was compared with the original unmodified HNN method as well as six state-of-the-art methods for LCCD. To explore the effect of uncertainty in spectral unmixing, which mainly originates from spectral separability in the input, coarse image, and the point spread function (PSF) of the sensor, a set of synthetic multispectral images with different class separabilities and PSFs was used in experiments. It was found that the proposed LCCD method (i.e., HNN with an FSRM) can separate more real changes from noise and produce more accurate LCCD results than the state-of-the-art methods. The advantage of the proposed method is more evident when the class separability is small and the variance in the PSF is large, that is, the uncertainty in spectral unmixing is large. Furthermore, the utilization of an FSRM can expedite the HNN-based processing required for LCCD. The advantage of the proposed method was also validated by applying to a set of real Landsat-Moderate Resolution Imaging Spectroradiometer (MODIS) images.

Index Terms—Hopfield neural network (HNN), land cover change detection (LCCD), subpixel mapping (SPM), super-resolution mapping.

I. INTRODUCTION

LAND COVER change detection (LCCD), one of the most important topics in remote sensing, has received increasing attention over the past decades [1]–[4]. With rapid changes on the Earth's surface, especially in highly developed areas, fine temporal resolution LCCD is becoming increasingly important.

Manuscript received April 24, 2014; revised June 30, 2014; accepted September 03, 2014. Date of publication September 21, 2014; date of current version March 27, 2015. This work was supported in part by the Research Grants Council, Hong Kong, under Grant PolyU 5249/12E, in part by the Ministry of Science and Technology of China under Grant 2012BAJ15B04 and Project 2012AA12A305, and in part by the National Natural Science Foundation of China under Grant 41331175. (*Corresponding author: Wenzhong Shi.*)

Q. Wang and Z. Li are with the Department of Land Surveying and Geo-Informatics, The Hong Kong Polytechnic University, Kowloon, Hong Kong (e-mail: wqm11111@126.com; lzbtonggi@gmail.com).

W. Shi is with The Hong Kong Polytechnic University, Kowloon, Hong Kong, and also with Wuhan University, Wuhan 430072, China (e-mail: lswzshi@polyu.edu.hk).

P. M. Atkinson is with Geography and Environment, University of Southampton, Highfield, Southampton SO17 1BJ, U.K. (e-mail: P.M.Atkinson@soton.ac.uk).

Color versions of one or more of the figures in this paper are available online at <http://ieeexplore.ieee.org>.

Digital Object Identifier 10.1109/JSTARS.2014.2355832

Meanwhile, it is often necessary to monitor land cover changes at a fine spatial resolution to provide sufficient detail for specific applications. Although sensors such as WorldView and GeoEye can capture images with a fine temporal and spatial resolution, the high cost limits their more general applications. Moreover, the narrow swath of these sensors cannot meet the demand of LCCD for large areas. It is, therefore, of great interest to conduct LCCD at both fine spatial and temporal resolutions using computer technologies.

For fine temporal resolution images with wide swath, such as the Moderate Resolution Imaging Spectroradiometer (MODIS) images, the spatial resolution is commonly coarse. For the purpose of fine spatial and temporal resolution LCCD, it is promising to obtain fine spatial resolution land cover information using downscaling techniques, by taking the fine temporal, but coarse spatial resolution images as inputs, possibly coupled with ancillary variables, such as images with fine spatial, but coarse temporal resolution.

Spatiotemporal fusion [5], also termed image blending in some remote sensing literature [6], is a common technique for fusing a coarse spatial, but fine temporal resolution image with a fine spatial, but coarse temporal resolution image to generate a fine spatial and temporal resolution image. Spatiotemporal fusion can be followed by standard LCCD techniques to achieve fine spatial and temporal resolution LCCD. However, spatiotemporal fusion is implemented based on the availability of at least one pair of fine-coarse spatial resolution images (e.g., Landsat-MODIS [7]) of the same area. The image pairs have to be acquired at a similar time to ensure almost zero changes between the scenes covered by the two different spatial resolution sensors. Considering cloud contamination and possible time inconsistency of image acquisitions [8], high quality image pairs can be difficult to obtain.

In coarse spatial resolution images, mixed pixels, which contain more than one land cover class, are a common problem. As a popular mixed pixel analysis technique, spectral unmixing has been studied for decades [9]. Spectral unmixing estimates the proportions of land cover classes within each mixed pixel, and the outputs of the coarse spatial, but fine temporal resolution image series can provide information on how much the proportion of each class changed during the studied period [10], [11]. However, spectral unmixing outputs are still at a coarse spatial resolution and cannot inform users of the LCCD information at a finer spatial resolution.

By taking the coarse proportions (i.e., unmixing outputs) as input, subpixel mapping (SPM) [12], also termed super-resolution mapping in the remote sensing community [13], has been developed for thematic mapping at a finer spatial

resolution (i.e., subpixel resolution) relative to the input image. In recent years, a variety of SPM algorithms have been developed, including genetic algorithms [14], particle swarm optimization [15], pixel swapping algorithm (PSA) [16]–[19], Hopfield neural network (HNN) [20]–[23], subpixel/pixel spatial attraction model (SPSAM) [24]–[28], back-propagation neural network [29]–[33], Kriging [34], indicator cokriging [35]–[38], Markov random field [39]–[44], contouring method [45]–[47], and interpolation-based methods [48]–[50].

SPM is a promising technique for fine spatial and temporal resolution LCCD and has increased its presence in LCCD [51]–[54]. Foody and Doan [51] applied the HNN-based SPM to detect forest cover changes in Brazil at the spatial resolution of Landsat data (i.e., 30 m) using two 300-m Medium Resolution Imaging Spectrometer-like images. For SPM of the coarse image on one date, Ling *et al.* [52] and Xu and Huang [53] modified the PSA, by incorporating the land cover information in a known fine spatial resolution land cover map (FSRM) from a former date. Li *et al.* [54] added a temporal energy function to a conventional Markov random field model to monitor forest changes in the Brazilian Amazon Basin at a subpixel resolution. However, the new model proposed in [54] introduces extra parameters (e.g., weights for the temporal energy function).

Spectral unmixing remains an open problem currently and the predicted pixel-level proportions are rarely perfect. The HNN has been used widely in SPM, appreciating the fact that the constraint of the HNN maintains as far as possible, but not slavishly, the original pixel-level proportions [55]. Therefore, in the HNN, errors from spectral unmixing can be alleviated to some extent. This is the advantage over PSA and other SPM algorithms that are coherent with the original pixel-level proportions. Furthermore, similar to the PSA, the HNN considers the interaction between subpixels and spatial dependence is described at the subpixel level. This character makes the HNN able to produce smooth SPM results, which is particularly suitable for homogeneous landscapes. Based on these advantages, in this paper, a new subpixel resolution LCCD algorithm based on the HNN is proposed. Different from [51], this paper considers borrowing information from an FSRM in a HNN-based SPM (in [51], the original HNN was used for SPM and no FSRM was used).

The SPM problem is under-determined and many multiple plausible solutions can lead to an equally coherent recreation of the input coarse proportion images. With auxiliary information, SPM can be enhanced and more changes from noise can be separated. In LCCD, it is important to take temporal information into account. FSRM carries reliable land cover information at the target fine spatial resolution and it is of great interest to include the temporal information from such data in subpixel resolution LCCD.

In the HNN model, the utilization of the FSRM may not only increase the SPM and LCCD accuracy, but also may expedite the implementation of the HNN. The approach to incorporating the FSRM information does not involve any new parameter. In contrast to spatiotemporal fusion, the proposed HNN with an FSRM method does not need a pair of fine-coarse spatial resolution images. Note that the novelty of the proposed method essentially lies in the SPM process and the subpixel resolution

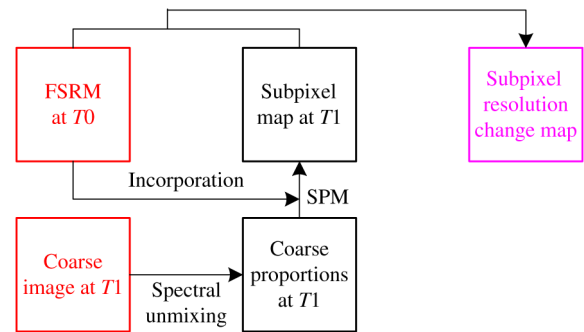


Fig. 1. Subpixel resolution LCCD problem.

LCCD is an application: the SPM result is compared with the FSRM for LCCD. The main contributions of this paper are, thus, as follows.

- 1) With the introduction of an FSRM, a new HNN model was proposed for subpixel resolution LCCD for the first time, in which the FSRM was used to initialize a part of neuron values (0 or 1 for each class) in the original HNN.
- 2) The effects of land cover class spectral separability [in terms of transformed divergence (TD)] on the accuracy of the proposed LCCD method were evaluated.
- 3) The effects of the point spread function (PSF) on the accuracy of the proposed LCCD method were evaluated.

The remainder of this paper is organized as follows. Section II first introduces the subpixel resolution LCCD problem (Section II-A), then the principle of the original HNN-based SPM method (Section II-B), and then incorporation of an FSRM in subpixel resolution LCCD (Section II-C), followed by the explicit description of the proposed HNN-based SPM for LCCD with an FSRM (Section II-D). Section III provides the experimental results, including comparison between the proposed LCCD method with the original HNN and state-of-the-art methods, analysis of the effects of TD and PSF on LCCD accuracy, and application to real Landsat-MODIS images. Further discussion is given in Section IV, while Section V concludes the paper.

II. METHODS

A. Subpixel Resolution LCCD Problem

Fig. 1 shows the subpixel resolution LCCD problem in this paper. The LCCD is conducted by using two input images covering the same scene (marked in red) with different spatial resolutions. One is a fine spatial resolution image FSRM at T_0 time, while the other is a coarse spatial resolution image at T_1 time. Spectral unmixing is first performed on the coarse image to estimate the proportions of each land cover class in the coarse pixels, and then SPM is conducted on the coarse proportion images to produce a fine spatial resolution (the same resolution as for the FSRM) thematic map. The subpixel map is compared with the FSRM for subpixel resolution LCCD. In SPM of the coarse image, the land cover information in the FSRM is incorporated into the SPM approach (i.e., HNN in this paper) to enhance the SPM.

B. HNN-Based SPM

Let (h, i, j) be a neuron in row i and column j [corresponds to subpixel (i, j)] of the network layer representing land cover class h , and v_{hij} be the output of the neuron. The output value means the value of class h ($h = 1, 2, \dots, K$, where K is the number of land cover classes) for subpixel (i, j) . If the output v_{hij} is 1, the subpixel (i, j) is allocated to class h , and if the neuron output value is 0, the subpixel does not belong to class h [56]. The HNN is used as an optimization tool to update iteratively the class values (i.e., v_{hij}) for each subpixel. The output v_{hij} is a function of the input signal u_{hij}

$$v_{hij} = \frac{1}{2} [1 + \tanh(\lambda u_{hij})] \quad (1)$$

where λ determines the steepness of the function. The input for the t th iteration is

$$u_{hij}(t + dt) = u_{hij} + \frac{du_{hij}(t)}{dt} dt \quad (2)$$

where dt is a time step. The second term on the right-hand side of (2) represents the energy change of the neuron and is described by

$$\frac{du_{hij}(t)}{dt} = -\frac{dE_{hij}}{dv_{hij}}. \quad (3)$$

The network energy function is

$$E = \sum_h \sum_i \sum_j (w_1 G1_{hij} + w_2 G2_{hij} + w_3 P_{hij} + w_4 M_{hij}) \quad (4)$$

where w_1, w_2, w_3 , and w_4 are four weights, $G1$ and $G2$ are two spatial clustering functions, P is the proportion constraint, and M is the multiclass constraint [21]. According to (4), the energy change in the neuron for subpixel (i, j) is determined by

$$\frac{dE_{hij}}{dv_{hij}} = w_1 \frac{dG1_{hij}}{dv_{hij}} + w_2 \frac{dG2_{hij}}{dv_{hij}} + w_3 \frac{dP_{hij}}{dv_{hij}} + w_4 \frac{dM_{hij}}{dv_{hij}}. \quad (5)$$

The first two terms of the right-hand side of (5) are expressed as

$$\frac{dG1_{hij}}{dv_{hij}} = \frac{1}{2} \left[1 + \tanh \left(\frac{1}{8} \sum_{\substack{b=i-1 \\ b \neq i}}^{i+1} \sum_{\substack{c=j-1 \\ c \neq j}}^{i+1} v_{hbc} - 0.5 \right) \lambda \right] (v_{hij} - 1) \quad (6)$$

$$\frac{dG2_{hij}}{dv_{hij}} = \frac{1}{2} \left[1 - \tanh \left(\frac{1}{8} \sum_{\substack{b=i-1 \\ b \neq i}}^{i+1} \sum_{\substack{c=j-1 \\ c \neq j}}^{i+1} v_{hbc} - 0.5 \right) \lambda \right] v_{hij}. \quad (7)$$

To increase the spatial correlation between neighboring subpixels, the function $G1$ increases the neuron output to 1, if the average output of the surrounding neurons is greater than

0.5, while function $G2$ decreases the neuron output to 0, if the average output of the surrounding neurons is less than 0.5.

The proportion constraint for class h is

$$\frac{dP_{hij}}{dv_{hij}} = \frac{1}{2S^2} \sum_{b=x \cdot S+1}^{x \cdot S+S} \sum_{c=y \cdot S+1}^{y \cdot S+S} [1 + \tanh(v_{hbc} - 0.5)\lambda] - F_{hxy} \quad (8)$$

where x and y are coordinates of the coarse pixel that subpixel (i, j) falls within, F_{hxy} is the coarse proportion of class h for pixel (x, y) , and S is the zoom factor (i.e., each coarse pixel is divided into $S \times S$ subpixels). The multiclass constraint means that for any subpixel, say (i, j) , the sum of neuron outputs for all classes should be equal to 1, thus

$$\frac{dM_{hij}}{dv_{hij}} = \left(\sum_{k=1}^K v_{kij} \right) - 1. \quad (9)$$

C. Incorporation of an FSRM in Subpixel Resolution LCCD

There is a temporal dependence between the images covering the same scene, especially for images acquired on close dates. These images are considered to resemble each other. The land cover information in the FSRM on one date ($T0$) can provide auxiliary information for SPM of the coarse spatial resolution image on a closer date ($T1$), thus, reducing errors in subpixel resolution LCCD. The principle of incorporating an FSRM in subpixel resolution LCCD is based on the comparison of spectral unmixing-derived class proportions with proportions obtained by degradation of the known FSRM. Guided by the proportion difference in a class at two different times, some locations at the subpixel scale are considered to be changed or unchanged for the class, and some subpixels are correspondingly considered to belong or not belong to the class. This can help to reduce the solution space of SPM and decrease the uncertainty in SPM. The incorporation of an FSRM in subpixel resolution LCCD includes the following steps [52].

- 1) The FSRM is degraded with an $S \times S$ mean filter to yield the coarse proportions of each class on that date, which is denoted as $F0_{hxy}$.
- 2) The spectral unmixing-derived class proportion is compared with the proportions obtained by the degradation of FSRM, and for any class, say h , the proportion difference Δ_{hxy} is calculated by

$$\Delta_{hxy} = F_{hxy} - F0_{hxy}. \quad (10)$$

Finally, the changed and unchanged subpixel locations for each class are determined, according to the following three rules.

- Rule 1)* If $\Delta_{hxy} < 0$, in coarse pixel (x, y) , subpixels for class h in the coarse image at $T1$ are within the area for class h in the FSRM at $T0$ (such as the gray area representing class h in Fig. 2), and some subpixels within that area are changed to other classes (i.e., non h classes in the white area).

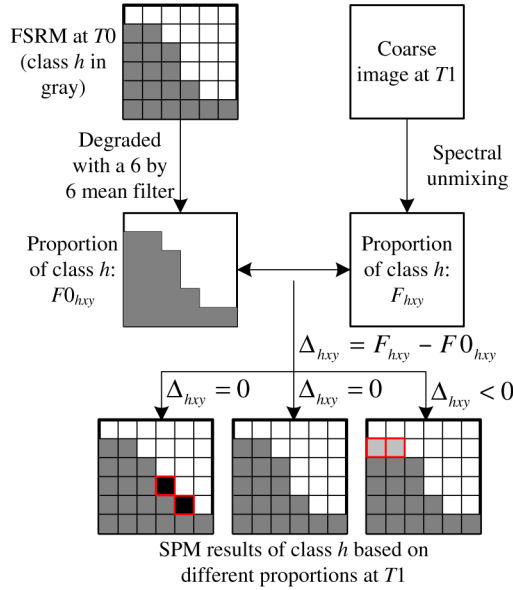


Fig. 2. Incorporation of an FSRM in subpixel resolution LCCD, where a single coarse pixel (x, y) and class h are used for illustration.

Rule 2) If $\Delta_{hxy} = 0$, in coarse pixel (x, y) , no change occurs for class h , and the spatial distribution of class h within coarse pixel (x, y) in the coarse image at $T1$ is the same as that in the FSRM at $T0$.

Rule 3) If $\Delta_{hxy} > 0$, in coarse pixel (x, y) , the locations of subpixels for class h in the FSRM (such as the gray area in Fig. 2) are assigned to class h in the coarse image at $T1$, and some subpixels at the remaining locations (i.e., the white area) are changed to class h .

At the bottom of Fig. 2, some examples are shown for three cases: $\Delta_{hxy} = 2/36$, $\Delta_{hxy} = 0$, and $\Delta_{hxy} = -2/36$. According to the corresponding hypothetical rules, at $T1$, two subpixels of non h class (e.g., the black subpixels in the left result) would be changed to class h , no changes occur for class h (middle result), and two subpixels of class h (e.g., the light gray subpixels in the right result) would be changed to non h classes. The key task of the SPM is to determine which subpixels in the white area are changed to class h when $\Delta_{hxy} > 0$ and which subpixels in the gray area are changed to non h classes when $\Delta_{hxy} < 0$. In this paper, this is achieved using the HNN approach, as illustrated in (1)–(9). The new HNN-based SPM for LCCD is introduced in the next section.

D. HNN for Subpixel Resolution LCCD With an FSRM

From the three rules in Section II-C, we can see that the determined changed and unchanged subpixel locations can be used to initialize the neuron values for each class in HNN-based SPM. The proposed HNN for subpixel resolution LCCD with an FSRM is performed based on the modification of neuron value initialization in the original HNN. For a coarse pixel (x, y) , let us divide all K classes into two groups:

one group consists of the classes with negative proportion differences (i.e., $\Delta < 0$), U_1, U_2, \dots, U_m , and the other group consists of the classes with nonnegative proportion differences (i.e., $\Delta \geq 0$), V_1, V_2, \dots, V_n , where $m + n = K$. To facilitate the illustration, we still use Fig. 2 as an example.

For classes U_1, U_2, \dots, U_m , according to Rule 1) in Section II-C, all subpixels for class U_h ($h = 1, 2, \dots, m$) in the coarse image at $T1$ fall within the area for class U_h in the FSRM at $T0$ (e.g., the gray area in Fig. 2), and all subpixels outside that area should not be assigned to class U_h . Following this rule, for classes U_1, U_2, \dots, U_m , the neuron outputs for the subpixels outside the “gray area” in the FSRM, these values are fixed for the network layers representing these classes.

For classes V_1, V_2, \dots, V_n , guided by the Rules 2) and 3), all subpixels within the area for class V_h ($h = 1, 2, \dots, n$) in the FSRM (e.g., the gray area in Fig. 2) should be assigned to class V_h in the coarse image at $T1$. With this in mind, for classes V_1, V_2, \dots, V_n , the neuron outputs for the subpixels within the “gray area” in the FSRM can be initialized to 1, which are fixed and do not involve iterative update for the network layers representing these classes.

After the modified initialization, the implementation of HNN-based SPM then becomes a prediction of neuron outputs of which the initialized values are not fixed. The steps of the proposed HNN for subpixel resolution LCCD with an FSRM are given below.

- 1) Spectral unmixing is performed on the coarse image at $T1$. The outputs are a set of coarse proportions $\{F_{hxy} | h = 1, 2, \dots, K; x = 1, 2, \dots, X; y = 1, 2, \dots, Y\}$, where X and Y are the rows and columns of the coarse image.
- 2) The spectral unmixing-derived proportion is compared with the proportion obtained by degrading the FSRM. The outputs are a set of proportion differences $\{\Delta_{hxy} | h = 1, 2, \dots, K; x = 1, 2, \dots, X; y = 1, 2, \dots, Y\}$.
- 3) According to the proportion differences, for each coarse pixel, all K classes are divided into two groups U_1, U_2, \dots, U_m and V_1, V_2, \dots, V_n . Neuron outputs for the two groups of classes are initialized, as shown in the pseudocode.
- 4) The HNN-based SPM is implemented. During the iterative process, the initialized values 0 and 1 in Step 3) are fixed and do not involve iterative update.
- 5) The predicted SPM result at $T1$ is compared with the FSRM at $T0$ in terms of class labels for LCCD.

As can be seen from Step 4), different from the original HNN, for each network layer representing a certain class, the new HNN model does not update the subpixel class values (i.e., neuron outputs) for the subpixels initialized with 0 or 1. Such scheme in the new HNN method can potentially help to decrease the computation burden. This is an obvious advantage of the proposed HNN method over the original HNN.

Algorithm: Initialization of HNN with an FSRM

Inputs: FSRM and $\{\Delta_{hxy} | h = 1, 2, \dots, K; x = 1, 2, \dots, X; y = 1, 2, \dots, Y\}$

for $x = 1: X$
for $y = 1: Y$

Find the classes with negative proportion differences (i.e., $\Delta < 0$), U_1, U_2, \dots, U_m , and the classes with nonnegative proportion differences (i.e., $\Delta \geq 0$), V_1, V_2, \dots, V_n .

for $h = 1: m$

For the network layer representing class U_h :

The neuron outputs for the subpixels outside the “gray area” in the FSRM (see Fig. 2) are set to 0;

The neuron outputs for the subpixels within the “gray area” in the FSRM are determined with a proportion-constrained initialization [20].

endfor

for $h = 1: n$

For the network layer representing class V_h :

The neuron outputs for the subpixels within the “gray area” in the FSRM (see Fig. 2) are set to 1;

The neuron outputs for the subpixels outside the “gray area” in the FSRM are determined with a proportion-constrained initialization.

endfor

endfor

endfor

Outputs: $\{v_{hij} | h = 1, 2, \dots, K; x = 1, 2, \dots, XS^2; y = 1, 2, \dots, YS^2\}$

III. EXPERIMENTS

In Sections III-A–III-E, the experiments were carried out on the synthetic multispectral images to study the effect of spectral unmixing errors (originating from the spectral separability and PSF in the images) in the proposed method. In Section III-F, a set of real Landsat-MODIS images covering a tropical forest area in Brazil was used to test the proposed method in a real case. For simplicity, we denote the original HNN-based SPM method [21], [51] as HNN1 and the new HNN method that borrows information from the FSRM as HNN2. For both HNN1 and HNN2, all the weighting constants in the network energy function were set to 1, the steepness of the *tanh* function was set to 10, the time step was set to 0.001, and the number of iterations was set to 1000. For HNN1, the proportion-constrained initialization was employed, as suggested in [20].

A. Data

The two original images were acquired by the Landsat-7 Enhanced Thematic Mapper sensor in August 2001 (T_0) and August 2002 (T_1) in the Liaoning Province, China. The spatial resolution is about 30 m. The studied area covers 240×240 pixels and four land cover classes, C1, C2, C3, and C4. Fig. 3

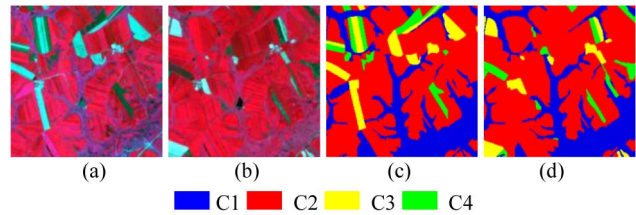


Fig. 3. Two images used in the experiments. The original images acquired in (a) August 2001 (T_0) and (b) August 2002 (T_1) (bands 4, 3, and 2 as RGB). (c) and (d) are the manually drawn reference maps of (a) and (b), respectively.

shows the two images and the corresponding manually digitized reference maps. The 30 m reference map at T_0 in Fig. 3(c) was used as the FSRM.

Spectral unmixing is a preprocessing step of SPM and the uncertainty from the former can be propagated directly to the latter. Moreover, from (10), we can see that the spectral unmixing outputs need to be compared with the proportions in the FSRM, and the proportion difference determines which rule in Section III-C should be used. Therefore, spectral unmixing plays an important role in the subpixel resolution LCCD method incorporating an FSRM. This necessitates the study of the effect of spectral unmixing errors in subpixel resolution LCCD. The uncertainty in spectral unmixing is closely related to spectral separability and PSF in remote sensing images.

To explore the effect of spectral unmixing in LCCD, we used synthetic multispectral images for time T_1 . First, the 30-m fine spatial resolution image at T_1 was synthesized, according to the reference land cover map in Fig. 3(d) and the predefined spectral separability (in terms of TD). The band number was set to three. Then the coarse spatial resolution image at T_1 was generated by degrading the synthesized fine spatial resolution (i.e., 30 m) images with an $S \times S$ mean filter, using a predefined PSF. To detect the changes at the fine spatial resolution, spectral unmixing and SPM were performed on the coarse image to reproduce the fine spatial resolution T_1 land cover map, which was compared with the FSRM for subpixel resolution LCCD. Using this setup, it was possible to synthesize coarse images with different spectral separabilities and PSFs, and thus, possible to analyze the effect of spectral separability and the PSF in the proposed method. Furthermore, the reference land cover map at fine spatial resolution at T_1 is known perfectly for accuracy assessment.

Concerning synthesizing the multispectral image at T_1 , the covariance matrix of the four classes was set to RI , where I is the identity matrix, and the constant $R = 10$. The mean value of C1 was set to a constant (100,100,100), and the mean values of the other three classes were correspondingly set to $(100 + \Delta\mu, 100, 100)$, $(100, 100 + \Delta\mu, 100)$, and $(100, 100, 100 + \Delta\mu)$, respectively, where $\Delta\mu$ is a function of the predefined TD [40]

$$\Delta\mu = \sqrt{-8R \ln(1 - TD/2)}. \quad (11)$$

TD is an index reflecting the spectral separability in remote sensing images. The separability between classes increases when the TD increases. Therefore, by tuning the TD values,

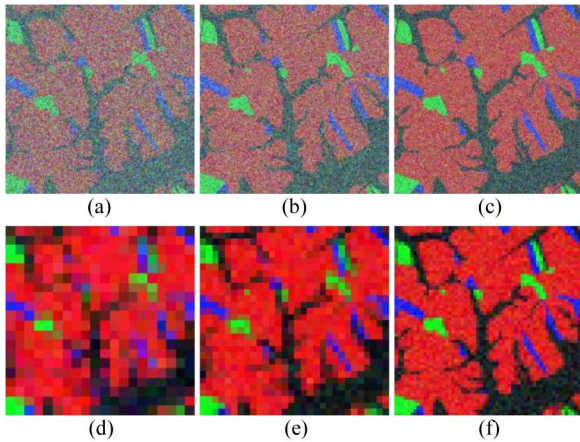


Fig. 4. Synthetic multispectral images. Fine spatial resolution images generated with (a) $TD = 0.5$, (b) $TD = 1$, and (c) $TD = 1.5$. Coarse spatial resolution images generated by degrading the fine spatial resolutions with (d) $TD = 0.5$, $S = 12$; (e) $TD = 1$, $S = 8$; and (f) $TD = 1.5$, $S = 4$.

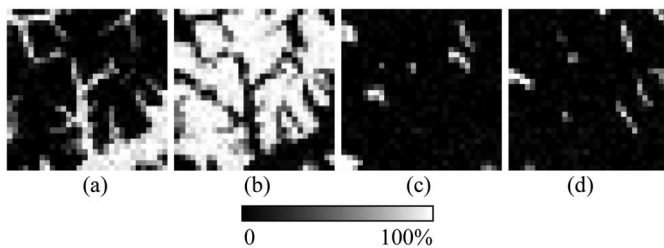


Fig. 5. Spectral unmixing results of the coarse image generated with $TD = 1$ and $S = 8$ for (a) C1, (b) C2, (c) C3, and (d) C4.

coarse images with different spectral separabilities can be synthesized. In the experiments, three different TD values were considered: 0.5, 1, and 1.5. Fig. 4 shows the synthetic images for different TD [PSF was not added in Fig. 4(d)–(f)].

B. Comparison Between Subpixel Resolution LCCD Methods

In this section, we compared the proposed HNN2 method with the original HNN1 method and another six subpixel resolution LCCD methods: PSA with the FSRM [52] and the five recently developed methods in [57] (i.e., bilinear interpolation, bicubic interpolation, SPSAM, Kriging, and radial basis function (RBF) interpolation [58] methods), which also incorporated the FSRM in LCCD. Fig. 4(e) produced with $TD = 1$ and $S = 8$ was considered as the coarse image at $T1$. The synthesized coarse image has a spatial resolution of 240 m, comparable with that for the MODIS image. Spectral unmixing was implemented on this coarse image and fully constrained least squares linear spectral mixture analysis [59] was employed. The estimated coarse proportion images of the four classes are shown in Fig. 5. Taking the proportion images as input, the eight SPM algorithms were then applied (zoom factor $S = 8$), and the SPM results at $T1$ were compared to the FSRM at $T0$ for subpixel resolution LCCD.

Fig. 6 shows the LCCD results for the eight SPM methods. As can be seen from the results, the bilinear interpolation, bicubic interpolation, SPSAM, Kriging, and RBF interpolation

methods generated some small patches and a scattering of noisy pixel values. Referring to the reference change map, it is clear that these pixels should belong to the unchanged area, but were recognized as changed pixels. For example, some pixels for C1 at $T0$ should still belong to C1 at $T1$, but were incorrectly classified as C4 (i.e., pixels for “C1 to C4” in the results). Although PSA produced more compact results than the other five methods, the small patches still exist. Compared with the PSA, bilinear, bicubic, SPSAM, Kriging, and RBF methods, HNN1 generated smoother and “cleaner” results, and some pixels of the pixels previously misclassified for unchanged areas were correctly classified. This is because the HNN model does not maintain perfectly the proportions derived by spectral unmixing, which themselves contain inherent errors. However, obvious errors exist in the HNN1 result. For example, some pixels were erroneously identified as “C1 to C2,” which appear as long blocky artifacts, as shown in the areas marked by the red line. The proposed HNN2, which borrowed land cover information from the FSRM, produced more satisfactory results than HNN1. This can be illustrated by the fact that there are noticeably fewer pixels incorrectly identified as “C1 to C2,” and the blocky artifacts for this category of change are much “thinner” than that in the HNN1 result (see the examples marked by the red line). Overall, the HNN2 method produced visually a more accurate LCCD result than the other seven subpixel resolution LCCD algorithms.

The overall accuracy (OA) for each method was calculated from the full-transition error matrix [60]. For the bilinear, bicubic, SPSAM, Kriging, and RBF methods, the OA was around 93.1%. The PSA and HNN1 methods have a similar OA of around 92.8%. The OA of the proposed HNN2 method was 94.86%, about 2% greater than the other seven methods.

C. Effects of Class Spectral Separability

Three images synthesized with three different TD values (i.e., 0.5, 1, and 1.5), as shown in Fig. 4(a)–(c), were considered in this section. Meanwhile, the coarse images were created with five different degradation factors: 4, 6, 8, 10, and 12. Correspondingly, the zoom factors of the SPM were set to $S = 4, 6, 8, 10,$ and 12 to restore the fine spatial resolution (i.e., 30 m) images at $T1$. Fig. 7 shows the OA of the subpixel resolution LCCD for four of the SPM methods: 1) RBF; 2) PSA; 3) HNN1; and 4) HNN2, with variable zoom factor S and TD . Note that the OA of LCCD of the other four SPM algorithms, bilinear interpolation, bicubic interpolation, SPSAM, and Kriging, is not shown in this figure, as they have similar OA to the RBF for all S and TD . Thus, the RBF method was selected as a representative for the five methods in [57]. From Fig. 7, three observations can be made.

First, consistent with the conclusion in Section III-B, the proposed HNN2 generally has greater accuracy than the other methods. The accuracy difference between HNN1 and HNN2 becomes more obvious when S increases. More precisely, the accuracy gain of HNN2 over HNN1 is small at $S = 4$, but increases steadily from around 0.6% at $S = 6$ to 2% at $S = 8$, 2.5%, at $S = 10$, and 3.5% at $S = 12$. The reason is that the uncertainty in SPM increases with increasing S , and with the

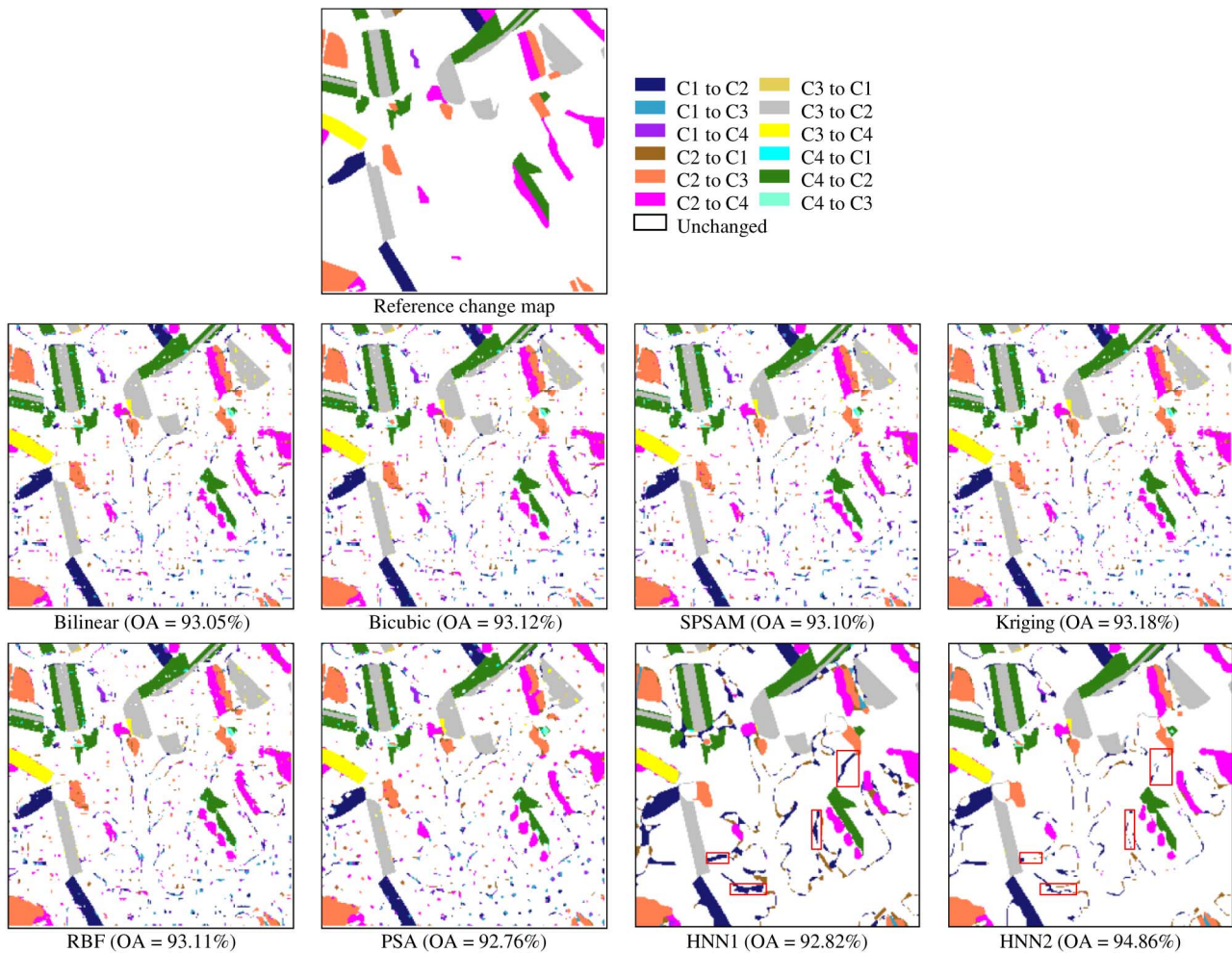


Fig. 6. Subpixel resolution LCCD results for the eight SPM methods.

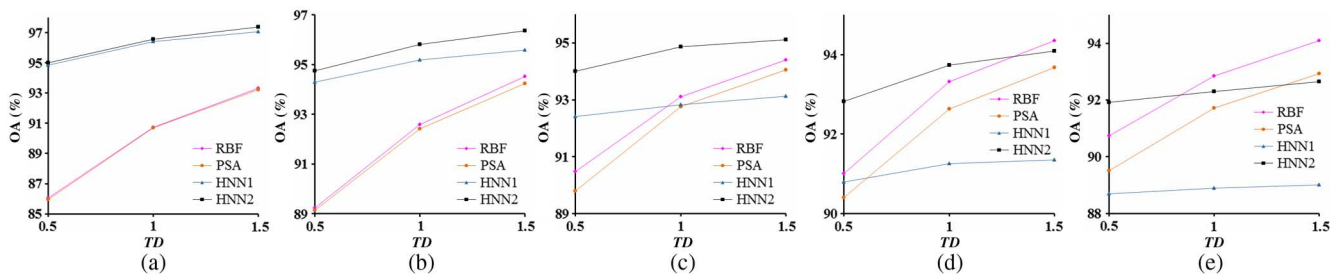


Fig. 7. OA of the subpixel resolution LCCD methods in relation to zoom factor S and TD . (a) $S = 4$, (b) $S = 6$, (c) $S = 8$, (d) $S = 10$, and (e) $S = 12$.

aid of the FSRM, HNN2 can reduce the solution space, thereby decreasing the uncertainty in SPM, especially for large S . This is not the case for HNN1 which was implemented based on the spatial dependence assumption without additional information.

Second, the OA of all methods increases when TD increases. This is because larger TD corresponds to greater class separability and the uncertainty in the preprocessing step of SPM (i.e., spectral unmixing) decreases correspondingly. This can be illustrated by the scatter-plots of the class proportions in Fig. 8, where the spectral unmixing results for $S = 8$ are provided. Focusing on the plots for three different TD values (the three rows), we find that from $TD = 0.5$ to $TD = 1.5$, the distribution of points for all four classes becomes more compact and

closer to the line of $y = x$ (x and y represent the horizontal and vertical axes), suggesting that the estimated proportions are closer to the actual proportions. Fig. 9 shows the corresponding spectral unmixing errors for Fig. 8 using the root-mean-square error (RMSE). When TD increases, the RMSE values of all four classes decrease.

Third, the advantage of the HNN2 over the RBF and PSA methods in terms of OA becomes less obvious when TD increases and is lost completely for a large zoom factor (e.g., $S = 12$). That is, the accuracy gains of RBF and PSA at large TD (e.g., $TD = 1.5$) are greater than that for HNN2. Two explanations can be made for this phenomenon: 1) as evident from Figs. 8 and 9, spectral unmixing error decreases with

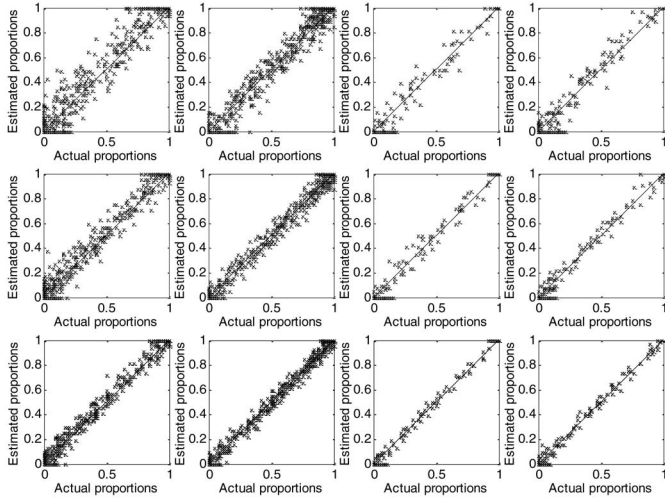


Fig. 8. Scatter-plots of class proportions for different TD ($S = 8$). The horizontal axis represents the reference class proportions, while the vertical axis represents the spectral unmixing-derived class proportions. Line 1: $TD = 0.5$; Line 2: $TD = 1$; Line 3: $TD = 1.5$. Left to right: C1, C2, C3, and C4.

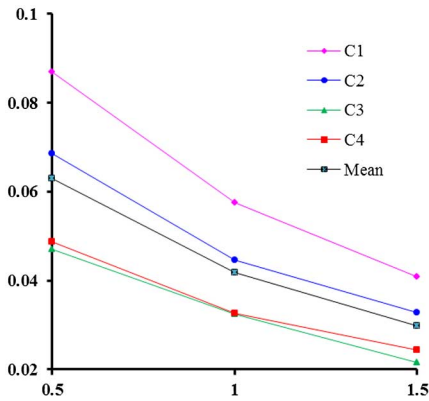


Fig. 9. Spectral unmixing errors (in terms of RMSE) in relation to TD ($S = 8$).

increasing TD . The greater accuracy gains of RBF and PSA with increasing TD arises because the two methods are more sensitive to the spectral unmixing accuracy, and compared with the postprocessing step (i.e., SPM), spectral unmixing plays a dominant role in their LCCD performances. This is not the case for the proposed HNN2, which can relax the proportion constraint; 2) both RBF and PSA utilized the FSRM in the experiments, and the benefits of using the FSRM for them are especially obvious for large zoom factor cases where large uncertainty exists in the SPM (as for each coarse pixel, the locations of more subpixel classes need to be predicted and uncertainty in the SPM increases).

D. Effects of PSF

The PSF inevitably exists in remote sensing data acquisition. It means that the signal for a given pixel is a function (in part) of spatial variation in neighboring pixels. As mentioned in [61], in the absence of a known PSF for the sensor involved, a suitable alternative would be to assume a Gaussian PSF. In this section, we used a Gaussian PSF, in which the size was 3×3 pixels and

the variance, denoted as D , was set to five values: 0.5, 0.75, 1, 1.25, and 1.5, respectively. Specifically, the image simulated with $TD = 1$ was degraded with an 8×8 mean filter, using the PSF with different D . Spectral unmixing was first performed on the simulated coarse images with different PSF, followed by the subpixel resolution LCCD methods ($S = 8$).

Fig. 10 shows the image generated using a PSF with $D = 0.75$ and its spectral unmixing results. Comparing Fig. 10(a) with Fig. 4(e), it can be seen that due to the existence of the PSF, the coarse image in Fig. 10(a) is visually more ambiguous and difficult to interpret. This is also the case in the estimated unmixing results in Fig. 10(b)–(e) when compared with Fig. 5(a)–(d). Taking Fig. 10 as input for SPM, the LCCD results produced by RBF, PSA, HNN1, and HNN2 are shown in Fig. 11. Comparing these results with Fig. 6, it can be seen that the PSF imposes negative effects on the subpixel resolution LCCD. Specifically, the RBF result in Fig. 11(a) contains obvious linear artifacts, and the PSA result in Fig. 11(b) contains larger size patches than the PSA result in Fig. 6. Regarding the HNN1 and HNN2 results, they are smoother than for the RBF method and there exist fewer misclassified pixels. Due to the effect of the PSF, however, more pixels are incorrectly classified as “C1 to C2” and “C2 to C1” in Fig. 11(c) and (d). Intercomparison of the four maps in Fig. 11 leads to the conclusion that the proposed HNN2 produces the most accurate LCCD result while accounting for the PSF effect.

The LCCD accuracy of the eight methods for the five variance values is exhibited in Fig. 12. Note that $D = 0$ means no PSF effect was added to the image simulation (i.e., the case studied in Section III-B). The results of $D = 0$ was included in Fig. 12 to illustrate the influence brought by the PSF in the subpixel resolution LCCD. Three observations can be made from the bar chart. First, HNN2 consistently produces the greatest accuracy among the eight LCCD methods for all five variance values and this advantage becomes more evident with increasing D . Second, the accuracy at $D = 0$ is greater than that of $D = 0.5, 0.75, 1, 1.25,$ and 1.5 . This means that the PSF imparts extra uncertainty in the subpixel resolution LCCD. Third, as D increases, the accuracy of all eight methods decreases. This is particularly evident when D increases from 0.5 to 0.75.

The last two observations necessitate the study of the influence of the PSF in spectral unmixing. Fig. 13 shows the scatter-plots of the spectral unmixing results for $D = 0, 0.75,$ and 1.5 . Without the PSF, the points are the most compact and the closest to the line of $y = x$. When D increases, the distribution becomes more scattered, which indicates an increase in spectral unmixing error. The spectral unmixing errors quantified (by the RMSE) for different D are displayed in Fig. 14. It can be observed clearly that the unmixing errors of all four classes increase as D increases. When D increases from 0.5 to 0.75, the errors of all four classes increase rapidly, and become stable from $D = 1.25$ to $D = 1.5$. With increasing D , the increased unmixing errors result in decreased LCCD accuracy. For example, from $D = 0.5$ to $D = 0.75$, the increased unmixing errors lead to an obvious decrease in the accuracy of LCCD (Fig. 12).

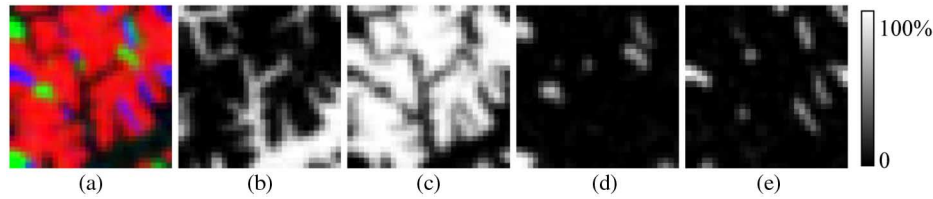


Fig. 10. Spectral unmixing results of the coarse image generated with $TD = 1$, $S = 8$, and $D = 0.75$. (a) The coarse image. (b)–(e) Proportion images of C1, C2, C3, and C4.

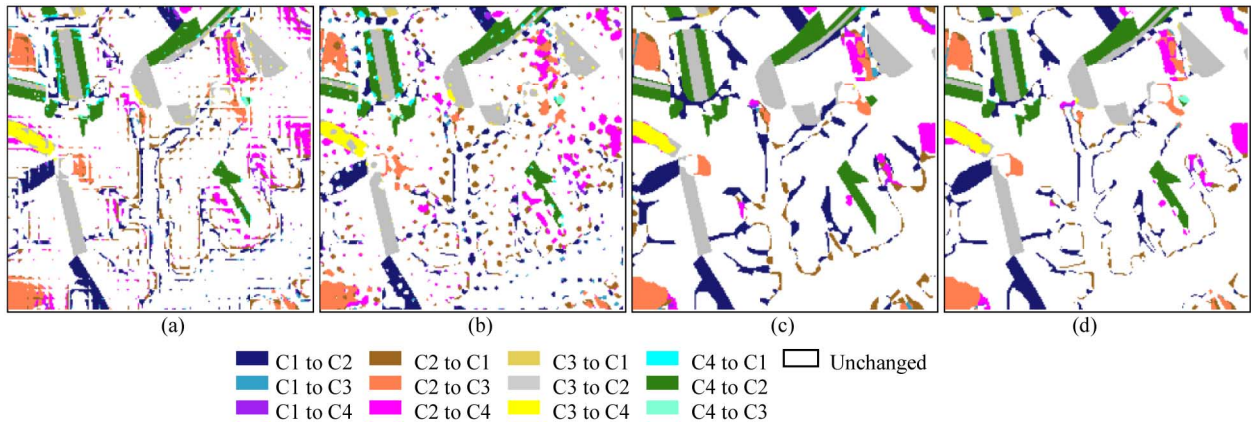


Fig. 11. Subpixel resolution LCCD results for the coarse image generated using a PSF with a variance $D = 0.75$ ($TD = 1$ and $S = 8$): (a) RBF, (b) PSA, (c) HNN1, and (d) HNN2.

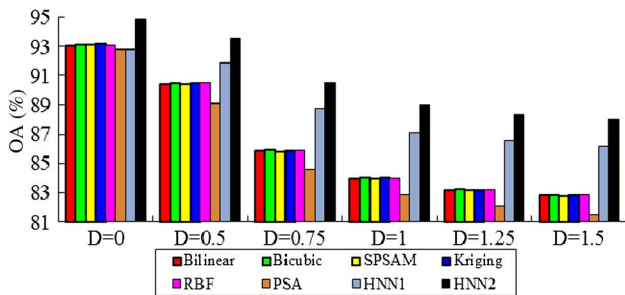


Fig. 12. OA of the eight LCCD methods in relation to the variance D in PSF ($TD = 1$ and $S = 8$).

E. Computing Efficiency

As mentioned in Section II-D, for each network layer representing a certain class, the HNN2 does not need to update the neuron outputs for the subpixels initialized with 0 or 1 from the FSRM. Theoretically, therefore, the HNN2 needs less computing time than HNN1. The computing times of PSA, HNN1, and HNN2 are listed in Table I. All experiments were tested on an Intel Core i7 Processor at 3.40-GHz with the MATLAB 7.1 version. PSA was implemented based on simulated annealing and the number of iterations was set to 2000. Note that the bilinear, bicubic, SPSAM, Kriging, and RBF methods are very fast subpixel resolution LCCD algorithms, as presented in [57]. In the experiments in this study, they took less than 3 s and they are much faster than the other three methods (i.e., PSA, HNN1, and HNN2). Examining the values in Table I, we find that PSA took much less time than HNN1 and HNN2. However, with the modified initialization from the FSRM, HNN2 is faster than HNN1.

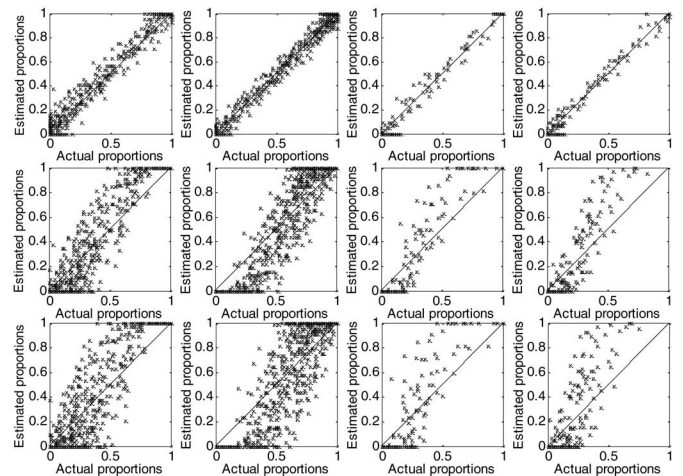


Fig. 13. Scatter-plots of class proportions for different variance D in PSF ($TD = 1$ and $S = 8$). The horizontal axis represents the reference class proportions, while the vertical axis represents the spectral unmixing-derived class proportions. Line 1: $D = 0$; Line 2: $D = 0.75$; Line 3: $D = 1.5$. Left to right: C1, C2, C3, and C4.

It should be mentioned that when S increases, PSA took less time, but HNN1 and HNN2 took more time. The reason is that PSA swaps subpixels within the coarse pixel and it is implemented in units of coarse pixels. With fixed iterations, the computing time of PSA is related mainly to the size of the coarse image. From $S = 4$ to $S = 12$ in the experiments in this paper, the size of the coarse images decreased from 60×60 pixels to 20×20 pixels. The HNN1 and HNN2 methods, however, are implemented in units of fine spatial resolution pixels (i.e., subpixels). Their computing time is, therefore, closely

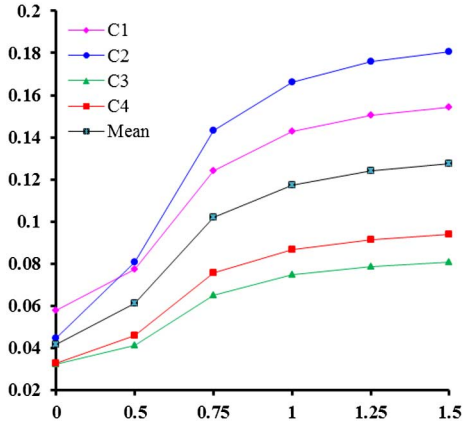


Fig. 14. Spectral unmixing errors (in terms of RMSE) in relation to the variance D in the PSF ($TD = 1$ and $S = 8$).

TABLE I
COMPUTING TIME (s) OF PSA, HNN1, AND HNN2 IN LCCD

	$S = 4$	$S = 6$	$S = 8$	$S = 10$	$S = 12$
PSA	259	130	77	54	41
HNN1	1871	2353	2804	3128	3755
HNN2	1620	1890	2100	2320	2500

related to the size of the map at the target fine spatial resolution, i.e., the number of subpixels for which the classes need to be predicted.

F. Application to Real Landsat-MODIS Images

The proposed method was applied to a set of real Landsat-MODIS images. The studied site is a $45 \text{ km} \times 45 \text{ km}$ area of tropical forest in Brazil. The land cover (mainly includes forest and nonforest) changes at the Landsat spatial resolution (i.e., 30 m) from July 1988 (T_0) to July 2005 (T_1) were detected, using a Landsat image acquired in July 1988 and a MODIS image acquired in July 2005. The Landsat image acquired in July 1988 was used as the source of the FSRM, and the SPM was conducted on a MODIS image acquired in July 2005 to produce the 30-m spatial resolution land cover map at T_1 . The original MODIS image was reprojected into a Universal Transverse Mercator and resampled to a spatial resolution of 450 m using the nearest-neighbor algorithm. The zoom factor for SPM was set to 15. The spatial size of the MODIS image is 100×100 pixels and the Landsat image is 1500×1500 pixels. The images are shown in Fig. 15.

For supervised assessment of SPM and LCCD, the other Landsat image acquired in July 2005 (T_1) was used as reference after registration. For each 30-m Landsat image, an unsupervised k -means classifier was employed to generate the 30-m fine spatial resolution thematic map. The 30 m T_0 map was used as the FSRM and the 30-m T_1 map was used as the reference for SPM. Spectral unmixing was implemented on the MODIS image, using fully constrained least squares linear spectral mixture analysis. The generated proportion images of forest and nonforest were used as input to the SPM. Table II is the LCCD accuracy of the eight methods. The accuracy of

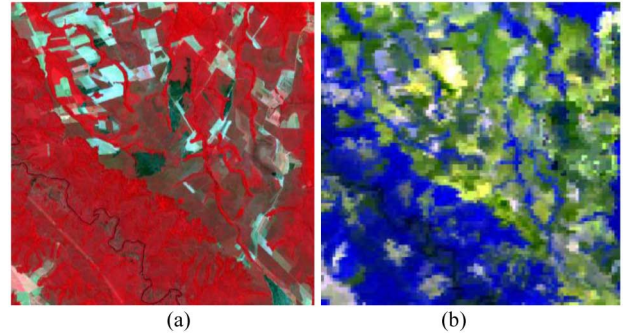


Fig. 15. Landsat-MODIS images (bands 4, 3, and 2 as RGB). (a) The Landsat image in July 1988. (b) The MODIS image in July 2005.

the decreased forest class for all eight methods is less than 60% and is the lowest among all four classes. However, the number of pixels for this class is only 5% of the whole scene and the relatively lower accuracy is not very influential on the OA. For the five methods in [57] and PSA method, the accuracy of all classes is generally lower than that of the two HNN methods. The OA of the six methods is around 75.5% and the two HNN methods produce greater OA (over 76% and over 77%) than the other six methods. With the FSRM, the HNN2 method produces greater accuracy for the two main classes (i.e., unchanged non-forest and unchanged forest) than for the HNN1 method. More precisely, for HNN2, the accuracy of the unchanged nonforest and unchanged forest is 1.5% and 2.5%, respectively, greater than that of HNN1, and correspondingly, the OA of HNN2 is 1.2% greater than that of HNN1.

IV. DISCUSSION

The experimental results demonstrate the effectiveness of the proposed subpixel resolution LCCD method with an FSRM. It is known that the evolution of land cover is complex in reality, and commonly, the temporal relation between images of the same scene decreases as the time interval increases. Approaches involving an FSRM are, thus, recommended as more suitable for change detection over short time intervals.

In Sections III-B and III-D, a set of MODIS-like coarse images was synthesized to test the LCCD methods. The encouraging results of the new HNN method suggest that it is potentially useful for reproducing 30-m spatial resolution Landsat-like thematic map information from a 240-m MODIS-like coarse image. With the inherent fine temporal resolution of MODIS images, the new method provides an interesting avenue for LCCD with both fine spatial and temporal resolutions. Furthermore, in Section III-C, we simulated coarse images with different spatial resolutions (i.e., by degrading the fine spatial resolution multispectral images with a factor ranging from 4 to 12) and the results suggested that the HNN with an FSRM method is advantageous for all coarse images. This reveals that the proposed method is applicable to remote sensing images with various spatial resolutions, not only MODIS images.

In the experiments, we synthesized coarse spatial resolution multispectral images with different spectral separabilities

TABLE II
ACCURACY (%) OF THE EIGHT LCCD METHODS FOR THE LANDSAT-MODIS IMAGES

	Bilinear	Bicubic	SPSAM	Kriging	RBF	PSA	HNN1	HNN2
Unchanged forest	73.97	73.93	73.96	73.94	73.93	74.02	71.57	74.00
Decreased forest	56.23	56.08	56.21	56.11	56.08	56.17	59.48	58.83
Increased forest	74.35	74.26	74.36	74.34	74.25	73.95	88.76	86.22
Unchanged non-forest	77.94	77.92	77.94	77.94	77.92	77.79	77.35	78.91
OA	75.51	75.47	75.50	75.49	75.47	75.38	76.36	77.55

and PSFs to simulate the uncertainty in spectral unmixing in real cases. The new HNN method was compared with seven benchmark algorithms, including the original HNN without an FSRM, PSA with an FSRM and five fast methods with an FSRM that were recently developed in [57]. The results show that the proposed HNN with an FSRM method produced consistently more accurate LCCD results than the other methods. The advantage is more obvious for a small TD value and large variance value in PSF, which corresponds to the case of large uncertainty in spectral unmixing. The unique advantage of the HNN-based method is that it does not slavishly maintain the proportion constraint, and the spatial clustering functions in the HNN can help to yield smooth SPM results. This is helpful to reduce the negative effect imposed by imperfect spectral unmixing (which mainly originates from spectral separability and the PSF) and separate real changes from noise. However, it should be mentioned that this character of the HNN makes the proposed method more appropriate for homogeneous landscape mapping (as was the case in the experiments), and it is not appropriate for restoring sharp edges of land cover at the subpixel level. Moreover, the spatial clustering function-based goal in the proposed HNN works well for the well-known H-resolution case (where the objects of interest are larger than the pixel size of the input coarse image). In cases where the objects of interest are smaller than the pixel size (i.e., the L-resolution case), the new method may lead to results with over-compact and over-large objects. Alternative prior spatial structure information based models, such as the model in [62], are more suited to, and should be applied in, the L-resolution case.

Although the proposed HNN with an FSRM method is capable of producing accurate LCCD results, the cost is the long computing time, as discussed in Section III-E. The five fast methods recently developed in [57] took only 3 s in the experiments. Users need to select appropriate SPM methods for LCCD according to their requirements. If the goal is increased accuracy, the proposed method is a preferable choice; if the goal is increased efficiency, the five fast methods in [57] are a preferable choice. In fact, the computing efficiency of the HNN-based SPM is closely related to the number of mixed pixels (along with the desired zoom factor). For pure pixels, the proportion-constrained initialization [20] can be used for neurons and the update in the HNN does not need to be undertaken for subpixels within pure pixels. We tested the proposed HNN with an FSRM (i.e., HNN2) and original HNN (i.e., HNN1) by using proportion images generated by degrading directly the reference land cover map in Fig. 3(d). The computing times are listed in Table III. The time in Table III is less than that

TABLE III
COMPUTING TIME (S) OF HNN1 AND HNN2 IN LCCD, WHERE PROPORTION IMAGES WERE SIMULATED BY DEGRADING THE REFERENCE LAND COVER MAP IN FIG. 3(D)

	$S = 4$	$S = 6$	$S = 8$	$S = 10$	$S = 12$
HNN1	600	957	1380	1737	2254
HNN2	205	344	503	610	862

in Table I. Without any uncertainty in spectral unmixing, more pure pixels can be correctly recognized and the number of subpixels for which the classes need to be predicted decreases, thus reducing the computing time. Another important observation from Table III is that the extent of the reduction in computing time for HNN2 is larger than that for HNN1. Analysis of Table III reveals that accurate spectral unmixing, especially accurate pure pixel recognition, is very helpful for reducing the computation burden of HNN, no matter whether an FSRM is used. In addition, HNN2 is again demonstrated to be more efficient than HNN1. The FSRM can, thus, be used to speed up the HNN. This is an important advantage of the proposed HNN2 over the original HNN1.

As indicated in (10), the spectral unmixing-derived proportions need to be compared with the proportions generated from the FSRM and the proportion difference determines which rule in Section II-C should be used in the proposed HNN-based subpixel LCCD method. The reliabilities of both proportions in (10) are important. In the experiments, we analyzed the uncertainty introduced by spectral unmixing, assuming that the FSRM is known perfectly. Although errors inevitably exist in spectral unmixing, which impart uncertainty in the calculation of the proportion difference in (10), the proposed method can still produce greater LCCD accuracy than the original HNN without the FSRM. In reality, the FSRM can be obtained by hard classification of the known fine spatial resolution image on one date, if such an image is available (similar to the premise of spatiotemporal fusion), or from some databases in a geographic information system (GIS). It would be an interesting topic to study the uncertainty in the FSRM in the proposed LCCD method.

As discussed above and analyzed in the experiments, spectral unmixing plays an important role in the proposed subpixel LCCD method, not only affecting LCCD accuracy but also computing efficiency. This calls for the application and exploration of more reliable spectral unmixing algorithms in LCCD, such as nonlinear unmixing [63] and multiple end-member spectral mixture analysis [64]. On the other hand, in [65],

with the acknowledgment that spectral unmixing is rarely perfect, for pixel-level LCCD, a threshold was set to determine the unchanged areas. This threshold may also be applied to subpixel resolution LCCD, which can help to detect more unchanged areas and reduce the computational burden of the proposed method. However, such a threshold needs to be determined with the availability of training information (i.e., fine spatial resolution training samples). These training samples need to be acquired on the same day as that of the coarse images for SPM. Determining how best to collect such training information is a challenging task for future research.

V. CONCLUSION

LCCD is becoming increasingly important for a wide range of applications, especially land cover and land use monitoring and planning. The Landsat TM and MODIS sensors are common sources of imagery used for change detection due to their free availability and regular revisit capabilities, but they provide coarse spatial resolutions relative to the requirements of certain applications (e.g., Landsat TM 30 m relative to changes in small residential buildings). There is, therefore, a great need for techniques that can produce fine spatial resolution change detection maps from such relatively coarse spatial resolution imagery.

In LCCD, it is always favorable to make use of temporal links between the images of the same scene. In this paper, we proposed a new HNN-based SPM method for subpixel resolution LCCD. The new method uses an FSRM on one date to enhance SPM from a coarse image on another, closer date. In the new HNN method, the FSRM is used for initialization of the neuron outputs, and the neurons fixed with 0 or 1 from the FSRM are not involved in the HNN iterative updating. The proposed method was tested with a set of synthetic multispectral images that were simulated according to different class separabilities (in terms of TD) and PSF, and a set of real Landsat-MODIS images. The conclusions from the experiments are summarized as follows.

- 1) With an FSRM, the proposed method produces consistently greater LCCD accuracy than the original HNN and state-of-the-art methods. The advantage over the original HNN becomes more obvious when the zoom factor desired for SPM increases.
- 2) The class separability affects the LCCD accuracy. When the class separability (in terms of TD) is small, the uncertainty in spectral unmixing is large, and this decreases the accuracy of all tested methods, including the proposed HNN with an FSRM method.
- 3) The PSF affects the LCCD accuracy. When the variance in the PSF (i.e., size of Gaussian PSF) is large, the uncertainty in spectral unmixing is large correspondingly, and the accuracy of all LCCD methods decreases.
- 4) The proposed method is more advantageous when the uncertainty in spectral unmixing is large (i.e., the class separability is small and the variance in the PSF is large).
- 5) With the modified initialization from the FSRM, the new HNN method is more computationally efficient than the original HNN method.

ACKNOWLEDGMENT

The authors would like to thank Mr. M. Hao of China University of Mining and Technology, Xuzhou, China, for providing the Liaoning Landsat dataset, Dr. X. Li of the Institute of Geodesy and Geophysics, Chinese Academy of Sciences, Wuhan, China, for kind discussion on synthesizing multispectral images and sharing the Brazil Landsat-MODIS dataset, and the anonymous reviewers for their valuable and constructive comments which have greatly improved the work.

REFERENCES

- [1] A. Singh, "Digital change detection techniques using remotely-sensed data," *Int. J. Remote Sens.*, vol. 10, no. 6, pp. 989–1003, 1989.
- [2] D. Lu, P. Mausel, E. Brondizio, and E. Moran, "Change detection techniques," *Int. J. Remote Sens.*, vol. 25, no. 12, pp. 2365–2407, 2004.
- [3] M. Hussain, D. Chen, A. Cheng, H. Wei, and D. Stanley, "Change detection from remotely sensed images: From pixel-based to object-based approaches," *ISPRS J. Photogramm. Remote Sens.*, vol. 80, pp. 91–106, 2013.
- [4] L. Bruzzone and F. Bovolo, "A novel framework for the design of change-detection systems for very-high-resolution remote sensing images," *Proc. IEEE*, vol. 101, no. 3, pp. 609–630, Mar. 2013.
- [5] X. Zhu, J. Chen, F. Gao, X. H. Chen, and J. G. Masek, "An enhanced spatial and temporal adaptive reflectance fusion model for complex heterogeneous regions," *Remote Sens. Environ.*, vol. 114, no. 11, pp. 2610–2623, 2010.
- [6] F. Gao, J. Masek, M. Schwaller, and F. Hall, "On the blending of the Landsat and MODIS surface reflectance: Predicting daily Landsat surface reflectance," *IEEE Trans. Geosci. Remote Sens.*, vol. 44, no. 8, pp. 2207–2218, Aug. 2006.
- [7] T. Hilker *et al.*, "A new data fusion model for high spatial- and temporal-resolution mapping of forest based on Landsat and MODIS," *Remote Sens. Environ.*, vol. 113, no. 8, pp. 1613–1627, 2009.
- [8] H. Song and B. Huang, "Spatiotemporal satellite image fusion through one-pair image learning," *IEEE Trans. Geosci. Remote Sens.*, vol. 51, no. 4, pp. 1883–1896, Apr. 2013.
- [9] J. M. Bioucas-Dias *et al.*, "Hyperspectral unmixing overview: Geometrical, statistical and sparse regression-based approaches," *IEEE J. Sel. Topics Appl. Earth Observ. Remote Sens.*, vol. 5, no. 2, pp. 354–379, Apr. 2012.
- [10] L. O. Anderson, Y. E. Shimabukuro, and E. Arai, "Multitemporal fraction images derived from Terra MODIS data for analysing land cover change over the Amazon region," *Int. J. Remote Sens.*, vol. 26, no. 11, pp. 2251–2257, 2005.
- [11] V. Haertel, Y. E. Shimabukuro, and R. Almeida, "Fraction images in multitemporal change detection," *Int. J. Remote Sens.*, vol. 25, no. 23, pp. 5473–5489, 2004.
- [12] P. M. Atkinson, "Issues of uncertainty in super-resolution mapping and their implications for the design of an inter-comparison study," *Int. J. Remote Sens.*, vol. 30, no. 20, pp. 5293–5308, 2009.
- [13] P. M. Atkinson, "Downscaling in remote sensing," *Int. J. Appl. Earth Observ. Geoinf.*, vol. 22, pp. 106–114, 2013.
- [14] K. C. Mertens, L. P. C. Verbeke, E. I. Ducheyne, and R. De Wulf, "Using genetic algorithms in sub-pixel mapping," *Int. J. Remote Sens.*, vol. 24, no. 21, pp. 4241–4247, 2003.
- [15] Q. Wang, L. Wang, and D. Liu, "Particle swarm optimization-based sub-pixel mapping for remote-sensing imagery," *Int. J. Remote Sens.*, vol. 33, no. 20, pp. 6480–6496, 2012.
- [16] P. M. Atkinson, "Sub-pixel target mapping from soft-classified, remotely sensed imagery," *Photogramm. Eng. Remote Sens.*, vol. 71, no. 7, pp. 839–846, 2005.
- [17] Y. Makido and A. Shortridge, "Weighting function alternatives for a sub-pixel allocation model," *Photogramm. Eng. Remote Sens.*, vol. 73, no. 11, pp. 1233–1240, 2007.
- [18] Z. Shen, J. Qi, and K. Wang, "Modification of pixel-swapping algorithm with initialization from a sub-pixel/pixel spatial attraction model," *Photogramm. Eng. Remote Sens.*, vol. 75, no. 5, pp. 557–567, 2009.
- [19] A. Villa, J. Chanussot, J. A. Benediktsson, C. Jutten, and R. Dambreville, "Unsupervised methods for the classification of hyperspectral images with low spatial resolution," *Pattern Recognit.*, vol. 46, pp. 1556–1568, 2013.

- [20] A. J. Tatem, H. G. Lewis, P. M. Atkinson, and M. S. Nixon, "Super-resolution target identification from remotely sensed images using a Hopfield neural network," *IEEE Trans. Geosci. Remote Sens.*, vol. 39, no. 4, pp. 781–796, Apr. 2001.
- [21] M. Q. Nguyen, P. M. Atkinson, and H. G. Lewis, "Superresolution mapping using a Hopfield neural network with fused images," *IEEE Trans. Geosci. Remote Sens.*, vol. 44, no. 3, pp. 736–749, Mar. 2006.
- [22] A. M. Muad and G. M. Foody, "Impact of land cover patch size on the accuracy of patch area representation in HNN-based super resolution mapping," *IEEE J. Sel. Topics Appl. Earth Observ. Remote Sens.*, vol. 5, no. 5, pp. 1418–1427, Oct. 2012.
- [23] M. Collins and M. De Jong, "Neuralizing target superresolution algorithms," *IEEE Geosci. Remote Sens. Lett.*, vol. 1, no. 4, pp. 318–321, Oct. 2004.
- [24] K. C. Mertens, B. D. Baset, L. P. C. Verbeke, and R. De Wulf, "A sub-pixel mapping algorithm based on sub-pixel/pixel spatial attraction models," *Int. J. Remote Sens.*, vol. 27, no. 15, pp. 3293–3310, 2006.
- [25] X. Tong, X. Zhang, J. Shan, H. Xie, and M. Liu, "Attraction-repulsion model-based subpixel mapping of multi-/hyperspectral imagery," *IEEE Trans. Geosci. Remote Sens.*, vol. 51, no. 5, pp. 2799–2814, May 2013.
- [26] X. Xu, Y. Zhong, and L. Zhang, "A sub-pixel mapping method based on an attraction model for multiple shifted remotely sensed images," *Neurocomputing*, vol. 134, pp. 79–91, 2014.
- [27] Y. Zhong and L. Zhang, "Remote sensing image subpixel mapping based on adaptive differential evolution," *IEEE Trans. Syst. Man Cybern. B. Cybern.*, vol. 42, no. 5, pp. 1306–1329, Oct. 2012.
- [28] Z. Mahmood, M. A. Akhter, G. Thoonen, and P. Scheunders, "Contextual subpixel mapping of hyperspectral images making use of a high resolution color image," *IEEE J. Sel. Topics Appl. Earth Observ. Remote Sens.*, vol. 6, no. 2, pp. 779–791, Apr. 2013.
- [29] K. C. Mertens, L. P. C. Verbeke, T. Westra, and R. De Wulf, "Sub-pixel mapping and sub-pixel sharpening using neural network predicted wavelet coefficients," *Remote Sens. Environ.*, vol. 91, pp. 225–236, 2004.
- [30] Y. Gu, Y. Zhang, and J. Zhang, "Integration of spatial-spectral information for resolution enhancement in hyperspectral images," *IEEE Trans. Geosci. Remote Sens.*, vol. 46, no. 5, pp. 1347–1358, May 2008.
- [31] D. Nigussie, R. Zurita-Milla, and J. G. P. W. Clevers, "Possibilities and limitations of artificial neural networks for subpixel mapping of land cover," *Int. J. Remote Sens.*, vol. 32, no. 22, pp. 7203–7226, 2011.
- [32] L. Zhang, K. Wu, Y. Zhong, and P. Li, "A new sub-pixel mapping algorithm based on a BP neural network with an observation model," *Neurocomputing*, vol. 71, no. 10–12, pp. 2046–2054, 2008.
- [33] Y. Shao and R. S. Lunetta, "Sub-pixel mapping of tree canopy, impervious surfaces, and cropland in the Laurentian great lakes basin using MODIS time-series data," *IEEE J. Sel. Topics Appl. Earth Observ. Remote Sens.*, vol. 4, no. 2, pp. 336–347, Jun. 2011.
- [34] J. Verhoeve and R. De Wulf, "Land-cover mapping at sub-pixel scales using linear optimization techniques," *Remote Sens. Environ.*, vol. 79, no. 1, pp. 96–104, 2002.
- [35] A. Boucher, P. C. Kyriakidis, and C. Cronkite-Ratcliff, "Geostatistical solutions for super-resolution land cover mapping," *IEEE Trans. Geosci. Remote Sens.*, vol. 46, no. 1, pp. 272–283, Jan. 2008.
- [36] Q. Wang, W. Shi, and L. Wang, "Indicator cokriging-based subpixel land cover mapping with shifted images," *IEEE J. Sel. Topics Appl. Earth Observ. Remote Sens.*, vol. 7, no. 1, pp. 327–339, Jan. 2014.
- [37] H. Jin, G. Mountrakis, and P. Li, "A super-resolution mapping method using local indicator variograms," *Int. J. Remote Sens.*, vol. 33, no. 24, pp. 7747–7773, 2012.
- [38] Q. Wang, P. M. Atkinson, and W. Shi, "Indicator cokriging-based sub-pixel mapping without prior spatial structure information," *IEEE Trans. Geosci. Remote Sens.*, vol. 53, no. 1, pp. 309–323, Jan. 2015.
- [39] T. Kasetkasem, M. K. Arora, and P. K. Varshney, "Super-resolution land-cover mapping using a Markov random field based approach," *Remote Sens. Environ.*, vol. 96, no. 3/4, pp. 302–314, 2005.
- [40] V. A. Tolpekin and A. Stein, "Quantification of the effects of land-cover-class spectral separability on the accuracy of Markov-random-field based superresolution mapping," *IEEE Trans. Geosci. Remote Sens.*, vol. 47, no. 9, pp. 3283–3297, Sep. 2009.
- [41] J. P. Ardila, V. A. Tolpekin, W. Bijker, and A. Stein, "Markov-random-field-based super-resolution mapping for identification of urban trees in VHR images," *ISPRS J. Photogramm. Remote Sens.*, vol. 66, pp. 762–775, 2011.
- [42] X. Li, F. Ling, Y. Du, and Y. Zhang, "Spatially adaptive superresolution land cover mapping with multispectral and panchromatic images," *IEEE Trans. Geosci. Remote Sens.*, vol. 52, no. 5, pp. 2810–2823, May 2014.
- [43] X. Li, Y. Du, and F. Ling, "Spatially adaptive smoothing parameter selection for Markov random field based sub-pixel mapping of remotely sensed images," *Int. J. Remote Sens.*, vol. 33, no. 24, pp. 7886–7901, 2012.
- [44] L. Wang and Q. Wang, "Subpixel mapping using Markov random field with multiple spectral constraints from subpixel shifted remote sensing images," *IEEE Geosci. Remote Sens. Lett.*, vol. 10, no. 3, pp. 598–602, May 2013.
- [45] G. M. Foody, A. M. Muslim, and P. M. Atkinson, "Super-resolution mapping of the waterline from remotely sensed data," *Int. J. Remote Sens.*, vol. 26, no. 24, pp. 5381–5392, 2005.
- [46] Y. F. Su, G. M. Foody, A. M. Muad, and K. S. Cheng, "Combining pixel swapping and contouring methods to enhance super-resolution mapping," *IEEE J. Sel. Topics Appl. Earth Observ. Remote Sens.*, vol. 5, no. 5, pp. 1428–1437, Oct. 2012.
- [47] Y. Ge, S. Li, and V. C. Lakhan, "Development and testing of a subpixel mapping algorithm," *IEEE Trans. Geosci. Remote Sens.*, vol. 47, no. 7, pp. 2155–2164, Jul. 2009.
- [48] F. Ling *et al.*, "Interpolation-based super-resolution land cover mapping," *Remote Sens. Lett.*, vol. 4, no. 7, pp. 629–638, 2013.
- [49] Q. Wang and W. Shi, "Utilizing multiple subpixel shifted images in sub-pixel mapping with image interpolation," *IEEE Geosci. Remote Sens. Lett.*, vol. 11, no. 4, pp. 798–802, Apr. 2014.
- [50] Q. Wang, W. Shi, and L. Wang, "Allocating classes for soft-then-hard subpixel mapping algorithms in units of class," *IEEE Trans. Geosci. Remote Sens.*, vol. 52, no. 5, pp. 2940–2959, May 2014.
- [51] G. M. Foody and H. T. X. Doan, "Variability in soft classification prediction and its implications for sub-pixel scale change detection and super-resolution mapping," *Photogramm. Eng. Remote Sens.*, vol. 73, no. 8, pp. 923–933, 2007.
- [52] F. Ling, W. Li, Y. Du, and X. Li, "Land cover change mapping at the subpixel scale with different spatial-resolution remotely sensed imagery," *IEEE Geosci. Remote Sens. Lett.*, vol. 8, no. 1, pp. 182–186, Jan. 2011.
- [53] Y. Xu and B. Huang, "A spatio-temporal pixel-swapping algorithm for subpixel land cover mapping," *IEEE Geosci. Remote Sens. Lett.*, vol. 11, no. 2, pp. 474–478, Feb. 2014.
- [54] X. Li, Y. Du, and F. Ling, "Super-resolution mapping of forests with bipeternal different spatial resolution images based on the spatial-temporal Markov random field," *IEEE J. Sel. Topics Appl. Earth Observ. Remote Sens.*, vol. 7, no. 1, pp. 29–39, Jan. 2014.
- [55] P. M. Atkinson, "Resolution manipulation and sub-pixel mapping," in *Remote Sensing Image Analysis: Including the Spatial Domain*, S. M. de Jong and F. D. van der Meer, Eds. Norwell, MA, USA: Kluwer, 2006, pp. 51–70.
- [56] A. J. Tatem, H. G. Lewis, P. M. Atkinson, and M. S. Nixon, "Multi-class land cover mapping at the sub-pixel scale using a Hopfield neural network," *Int. J. Appl. Earth Observ. Geoinf.*, vol. 3, no. 2, pp. 184–190, 2001.
- [57] Q. Wang, P. M. Atkinson, and W. Shi, "Fast sub-pixel mapping algorithms for sub-pixel resolution change detection," *IEEE Trans. Geosci. Remote Sens.*, vol. 53, no. 4, Apr. 2015, doi: 10.1109/TGRS.2014.2346535.
- [58] Q. Wang, W. Shi, and P. M. Atkinson, "Sub-pixel mapping of remote sensing images based on radial basis function interpolation," *ISPRS J. Photogramm. Remote Sens.*, vol. 92, pp. 1–15, 2014.
- [59] L. Wang, D. Liu, and Q. Wang, "Geometric method of fully constrained least squares linear spectral mixture analysis," *IEEE Trans. Geosci. Remote Sens.*, vol. 51, no. 6, pp. 3558–3566, Jun. 2013.
- [60] R. D. Macleod and R. G. Congalton, "A quantitative comparison of change-detection algorithms for monitoring eelgrass from remotely sensed data," *Photogramm. Eng. Remote Sens.*, vol. 64, no. 3, pp. 207–216, 1998.
- [61] F. D. van der Meer, "Remote-sensing image analysis and geostatistics," *Int. J. Remote Sens.*, vol. 33, no. 18, pp. 5644–5676, 2012.
- [62] A. J. Tatem, H. G. Lewis, P. M. Atkinson, and M. S. Nixon, "Super-resolution land cover pattern prediction using a Hopfield neural network," *Remote Sens. Environ.*, vol. 79, pp. 1–14, 2002.
- [63] A. Halimi, Y. Altmann, N. Dobigeon, and J. Y. Tourneret, "Nonlinear unmixing of hyperspectral images using a generalized bilinear model," *IEEE Trans. Geosci. Remote Sens.*, vol. 49, no. 11, pp. 4153–4162, Nov. 2011.
- [64] X. Jia and L. Wang, "Fuzzy assessment of spectral unmixing algorithms," *IEEE J. Sel. Topics Appl. Earth Observ. Remote Sens.*, vol. 7, no. 6, pp. 1947–1955, Jun. 2014, doi: 10.1109/JSTARS.2013.2264313.
- [65] D. Lu, M. Batistella, and E. Moran, "Multitemporal spectral mixture analysis for Amazonian land-cover change detection," *Can. J. Remote Sens.*, vol. 30, no. 1, pp. 87–100, 2004.



Qunming Wang received the B.S. and M.S. degrees from Harbin Engineering University, Harbin, China, in 2010 and 2012, respectively, and is currently pursuing the Ph.D. degree at the Department of Land Surveying and Geo-Informatics, The Hong Kong Polytechnic University, Kowloon, Hong Kong.

From June to December 2013, he was a visiting Ph.D. student in Geography and Environment, University of Southampton, U.K. His research interests include remote sensing image analysis, geostatistics, and pattern recognition.

Mr. Wang has published 20 peer-reviewed articles in international journals such as IEEE TRANSACTIONS ON GEOSCIENCE AND REMOTE SENSING, *ISPRS Journal of Photogrammetry and Remote Sensing*, and IEEE JOURNAL OF SELECTED TOPICS IN APPLIED EARTH OBSERVATION AND REMOTE SENSING. He serves as a Reviewer for over 10 international journals, including IEEE TRANSACTIONS ON GEOSCIENCE AND REMOTE SENSING, IEEE TRANSACTIONS ON CYBERNETICS, IEEE GEOSCIENCE AND REMOTE SENSING LETTERS, IEEE JOURNAL OF SELECTED TOPICS IN APPLIED EARTH OBSERVATION AND REMOTE SENSING, PHOTOGRAMMETRIC ENGINEERING AND REMOTE SENSING, and *International Journal of Remote Sensing*. He was the recipient of the Excellent Master Dissertation Award and the Excellent Graduates in Heilongjiang Province, China, in 2012. He has been awarded the Hypercompetitive Hong Kong Ph.D. Fellowship.



Wenzhong Shi obtained the Ph.D. degree from the University of Osnabrück, Vechta, Germany, in 1994.

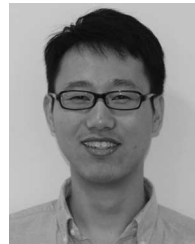
He is a Chair Professor in GIS and remote sensing, Department of Land Surveying and Geo-Informatics, The Hong Kong Polytechnic University, Kowloon, Hong Kong. He has published over 100 SCI papers and 10 books. His research interests include GIS and remote sensing, uncertainty and spatial data quality control, image processing for high-resolution satellite images.

Prof. Shi received the State Natural Science Award from the State Council of China in 2007 and The Wang Zhizhuo Award from International Society for Photogrammetry and Remote Sensing in 2012.



Peter M. Atkinson received the B.Sc. degree in geography from the University of Nottingham, Nottingham, U.K., in 1986, the Ph.D. degree from the University of Sheffield (NERC CASE award with Rothamsted Experimental Station), South Yorkshire, U.K., in 1990, and the M.B.A. degree from the University of Southampton, Southampton, U.K., in 2012.

Currently, he is a Professor of Geography with the University of Southampton. He has published over 170 peer-reviewed articles in international scientific journals and around 50 refereed book chapters. He has also edited nine journal special issues and eight books. He has organized several major international conferences in Southampton including GeoComputation in 2003 and GeoENV in 2008. He is an Associate Editor for *Computers and Geosciences* and sits on the editorial boards of several further journals including *Geographical Analysis*, *Spatial Statistics*, the *International Journal of Applied Earth Observation and Geoinformation*, and *Environmental Informatics*. He sits on various international scientific committees. His research interests include remote sensing, geographical information science, and spatial (and space-time) statistics applied to a range of environmental science and socioeconomic problems.



Zhongbin Li (S'13) received the M.S. degree in surveying engineering from Tongji University, Shanghai, China, in 2012, and is currently pursuing the Ph.D. degree at the Department of Land Surveying and Geo-Informatics, The Hong Kong Polytechnic University, Kowloon, Hong Kong.

He serves as a referee for *European Journal of Remote Sensing*, IEEE GEOSCIENCE AND REMOTE SENSING LETTERS, and IEEE JOURNAL OF SELECTED TOPICS IN APPLIED EARTH OBSERVATIONS AND REMOTE SENSING. His research

interests include partial differential equation for image processing, image matting, and machine learning.